

# Scalable topological quantum computing based on Sine-Cosine chain models

A. Lykholat<sup>1</sup>, G. F. Moreira<sup>1</sup>, I. R. Martins<sup>2</sup>, D. Sousa<sup>3</sup>,  
A. M. Marques<sup>1</sup>, R. G. Dias<sup>1\*</sup>

<sup>1</sup>Department of Physics & i3N, University of Aveiro,  
3810-193 Aveiro, Portugal

<sup>2</sup>Laboratório de Instrumentação e Física Experimental de Partículas (LIP),  
Universidade do Minho, 4710-057 Braga, Portugal

<sup>3</sup>Max-Planck-Institute for Solid State Research, Heisenbergstrasse 1,  
70569 Stuttgart, Germany

\*rdias@ua.pt

## Abstract

This work proposes a scalable framework for topological quantum computing using Matryoshka-type Sine-Cosine chains. These chains support high-dimensional qudit encoding within single systems, reducing the physical resource overhead compared to conventional qubit arrays. We describe how these chains can be used in Y-junction braiding protocols for gate operations and in extended memory architectures capable of storing multiple qubits simultaneously. Fidelity analysis shows partial topological protection against disorder, suggesting this approach is a possible pathway toward low-overhead quantum hardware.

## 1 Introduction

Practical quantum computing has been limited by the nature of quantum states, which are susceptible to environmental interactions that cause decoherence and information loss [1, 2]. Despite decades of progress, current architectures, primarily superconducting qubits requiring cooling [3, 4], struggle with scalability. Physical resource overhead from error mitigation (constructing logical qubits from multiple physical qubits and implementing quantum error correction) complicates large-scale implementations, making fault-tolerant operation difficult as system sizes grow [5, 6]. These challenges motivate alternative approaches to protecting information through topological rather than physical isolation [7, 8].

Square-root topological insulators ( $\sqrt{\text{TI}}$ ) represent a unique class of systems where topological features are hidden until the Hamiltonian is squared, revealing a "parent" topological insulator [9, 10]. This hidden relationship means that the edge states of the  $\sqrt{\text{TI}}$  actually retain partially the topological protection of the parent's zero-energy edge states.  $2^n$ -root topological insulators generalize this logic by adding  $n$  layers of squaring operations (and energy shifts) [11, 12, 13], creating a recursive structure often visualized as an arborescence [12] or, for the specific Sine-Cosine models addressed in this paper, a Matryoshka sequence [13]. The construction of these models is the inverse of the squaring process, that is, a square-root operation that typically involves combining the lattice with the respective line graph and carefully adjusting hopping parameters between sublattices in order to keep onsite potentials uniform in one sublattice when squaring. As the root degree  $n$  grows, the system gains many edge states, but the original topological protection becomes more diluted. By encoding multiple qubits or qudits within a such single topological system, we can significantly reduce physical resource overhead while maintaining robustness against local perturbations.

This paper addresses a particular  $2^n$ -root one-dimensional topological insulator, the Matryoshka model [13], which is constructed by recursively applying a square-root operation to the SSH chain [14]. This process creates a lattice with staggered sine-cosine hopping terms, resulting in a significantly larger number of energy gaps and edge states. Our paper details applications of this model in (i) quantum state transfer, (ii) quantum gate, and (iii) quantum memories by basically showing that the square-root operation can still be applied to known implementations of quantum state transfer [15, 16, 17], quantum

gate [18], and quantum memories [19, 20] in the SSH chain. We also analyze the robustness of our protocols against various types of disorder (on-site, off-diagonal, and correlated disorder).

This paper is organized as follows. Section 2 defines the Matryoshka chain, detailing its Hamiltonian construction, recursive square-root logic, energy dispersion relations, and the resulting edge states. Section 3 describes protocols for quantum state transfer in these chains via defect motion. Section 4 describes scalable Y-junction braiding for gate operations and analyzes robustness against various types of disorder. Section 5 extends the analysis to quantum memory architectures, explaining how protected edge states enable qubit (or qudit) storage and retrieval using Rabi oscillations. The conclusion summarizes the proposed scalability benefits and potential experimental realizations in photonic or circuit systems. Appendices A, B, and C provide mathematical derivations for transfer protocols, robustness against level crossing and disorder, and extensions to multi-qubit or qudit memory, respectively.

## 2 The Matryoshka Model

In this section, we introduce the Matryoshka model [13], which can support significantly more edge states than the SSH chain and has potential applications in many-qubit hardware architectures, as we will show later. A Matryoshka chain is composed of a sequence of sine and cosine hopping terms in the following way,

$$H = t^{(P)} \sum_{m=1}^N \left[ \sum_{j=1}^{2^P} \sin \theta_j |m, B_j\rangle \langle m, A_j| + \sum_{j=1}^{2^P-1} \cos \theta_j |m, A_{j+1}\rangle \langle m, B_j| + \cos \theta_{2^P} |m+1, A_1\rangle \langle m, B_{2^P}| \right] + H.c., \quad (1)$$

where  $P$  is the structure order,  $N$  represents the number of unit cells and  $t^{(P)}$  is the energy scale. The number of distinct angles  $\theta_j$  can grow indefinitely in sequences of  $2^P$  as shown in Fig. 1.

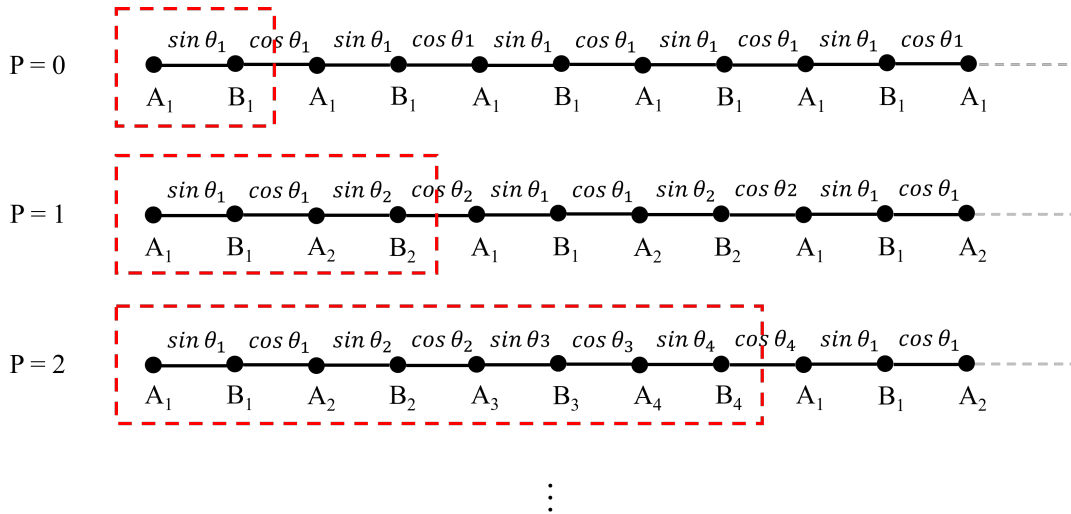


Figure 1: Lattice representation of the first orders of  $P$  in the Matryoshka model. The figure illustrates how the unit cell evolves for  $P = 0, 1, 2$ , becoming progressively larger as we increase  $P$ , with hopping terms given by sine and cosine functions of angles  $\theta_j$ .

Note that system  $P = 0$ , which supports only two connection values,  $\sin \theta_1$  and  $\cos \theta_1$ , corresponds exactly to the SSH chain, with an energy gap at the center of the spectrum. Now, analyzing the chain with  $P = 1$  order, with a total of two alternating angles,  $\theta_1$  and  $\theta_2$ , we can decompose this lattice into two sublattices by squaring its Hamiltonian. Using the chiral basis  $\{|m, A_j\rangle, |m, B_j\rangle\}$ , with  $j = 1, 2, \dots, 2^P$  and  $m = 1, 2, \dots, N$ , we obtain for general  $P$

$$H_P^2 = \begin{pmatrix} H_A & 0 \\ 0 & H_B \end{pmatrix}. \quad (2)$$

In the case  $P = 1$ , the representation of  $H_B$  will correspond to a bipartite structure corresponding to  $P = 0$  with a global energy offset of 1 (red sites in Fig. 2), while  $H_A$  is a residual chain that has the same finite energy spectrum [9] but manifests non-uniform on-site potentials along its matrix diagonal (blue and green sites in Fig. 2). Since  $H_{P=0}$  and  $H_B$  energy spectra are the same (apart from the energy

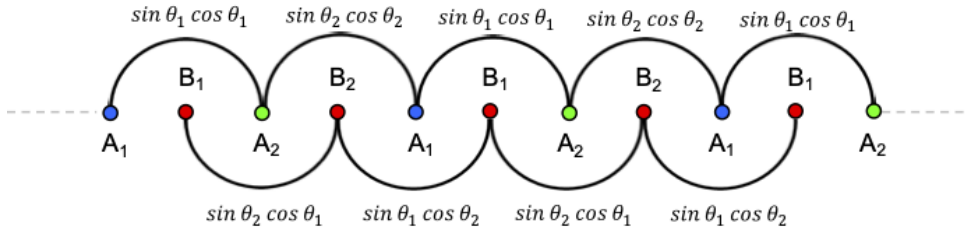


Figure 2: Representation of the resulting structures  $H_A$  and  $H_B$  after applying the squaring operation to the parent Hamiltonian. The diagram illustrates the separation into two decoupled sublattices, with effective hoppings dependent on the parameters  $\theta_1$  and  $\theta_2$ .

shift), we have (for general  $P$ ) the following conditions:

$$t^{(P-1)} \sin \theta_j^{(P-1)} = \sin \theta_{2j-1}^{(P)} \cos \theta_{2j}^{(P)}, \quad (3)$$

$$t^{(P-1)} \cos \theta_j^{(P-1)} = \sin \theta_{2j}^{(P)} \cos \theta_{2j+1}^{(P)}, \quad (4)$$

$$t^{(P-1)} = \sqrt{(\sin \theta_{2j-1}^{(P)} \cos \theta_{2j}^{(P)})^2 + (\sin \theta_{2j}^{(P)} \cos \theta_{2j+1}^{(P)})^2}, \quad (5)$$

with  $j = 1, \dots, 2^P$ .

The  $P = 0$  energy dispersion relation is  $E_{\pm}(k) = \pm\sqrt{1 + \sin 2\theta \cos k}$ , and for general  $P$  we have the multi-band energy spectrum

$$E_{\pm\pm\dots\pm}(k)^{(P)} = \pm\sqrt{1 + t^{(P-1)} E_{\pm\pm\dots\pm}(k)^{(P-1)}}. \quad (6)$$

where the term  $E_{\pm\pm\dots\pm}(k)^{(P)}$  has  $P + 1$  signs and all the possible combinations of signs must be considered. From the last expression, one can understand that the number of energy bands grows with the order of  $P$ , such that  $\#_{E^{(P)}} = 2\#_{E^{(P-1)}} = 2^{P+1}$ , with an energy offset of 1 after each squaring operation. All the energy spectra present chiral symmetry, as one can see in Fig. 3.

The existence of weak links at the chain ends in any structure of type  $P$  implies that two degenerate (ignoring finite size corrections) edge states of energy  $E = 0$  exist in its spectrum. Each of these zero energy levels unfolds into two in the next structure spectrum  $P + 1$ . When applying correlated disorder on  $\theta_j$  values, chiral symmetry preserves the protection of the edge states hosted in the gaps, with energies

$$\begin{aligned} & \pm 1, \quad \pm\sqrt{1 \pm t^{(P-1)}}, \quad \pm\sqrt{1 \pm t^{(P-1)}}\sqrt{1 \pm t^{(P-2)}}, \\ & \dots \quad \pm\sqrt{1 \pm t^{(P-1)}}\sqrt{1 \pm t^{(P-2)}}\sqrt{\dots}\sqrt{1 \pm t^{(1)}}. \end{aligned} \quad (7)$$

To summarize, whenever the order of  $P$  is increased, we double the total amount of energy bands, the total number of band gaps becomes to  $2^{P+1} - 1$ , and each gap can host 2 edge states, allowing up to  $2^{P+2} - 2$  edge states to appear in the energy spectrum under OBC.

### 3 Quantum Transfer in a Matryoshka Type Chain

The search for scalable quantum information processing and reliable quantum communication has motivated the study of quantum state transfer in quantum chains in recent years [16, 21, 22, 17, 15, 18]. In one-dimensional topological models, such as the Su-Schrieffer-Heeger (SSH) model, the transport of a particle from one side of a chain to the opposite side can be mediated by topologically protected edge states, which provide robustness against disorder and environmental noise [22, 17, 23]. In particular, the quantum-state-transfer protocol of [18] relies on the adiabatic motion of a defect (a localized

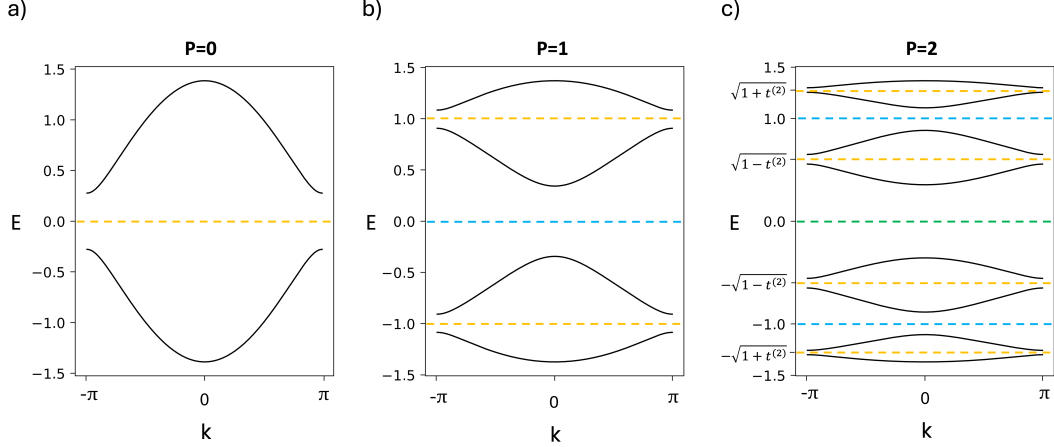


Figure 3: Band structure of a)  $P = 0$ , b)  $P = 1$  and c)  $P = 2$  Matryoshka chain. To calculate the base lattice ( $P = 0$ ) energies,  $\sin \theta_1 = 0.588$  was used. To obtain the next lattice's band structure  $t^{(0)} = 0.9/\sqrt{2}$  and  $t^{(1)} = 0.8/\sqrt{2}$  were used. The yellow line represents the edge states relative to the weak links of  $P = 0$ , which double after each squaring. In the case that  $P = 0$  does not present weak links, none of the yellow lines can be seen in the spectra. This same logic applies to the degenerate blue states in  $P = 1$ , which unfold and form two in  $P = 2$ . The green line corresponds to the weak links for  $P = 2$ .

zero-energy mode) along a 3-site SSH chain as illustrated in Fig. 4(a). In this section, we show that in a Matryoshka chain, the same defect–transfer mechanism applies because the square-root construction of the Matryoshka chain implies that its eigenvectors are built on the underlying eigenvectors of the 3-site SSH chain. Below, we outline the mapping between the parent and the square-root chain, the adiabatic conditions, and the protocol that can be implemented directly in a Matryoshka lattice.

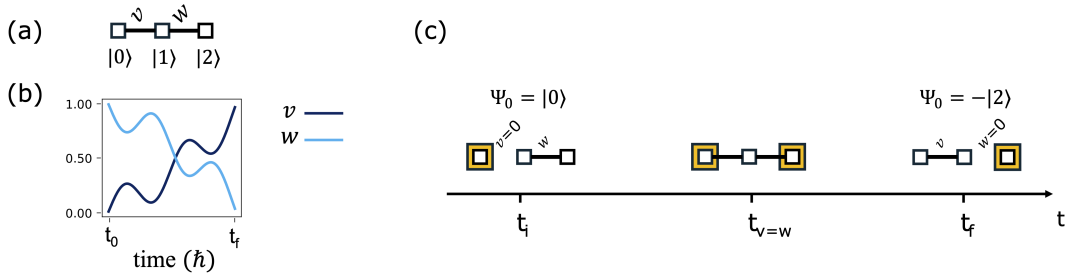


Figure 4: In this figure, we reproduce the transferring protocol of [18]. (a) Base system. (b) Adiabatic sweep of the couplings  $v(t)$  and  $w(t)$ . (c) Transfer protocol illustration. The yellow squares indicate finite state amplitudes. When  $v = 0$  we have  $|\Psi(t_i)\rangle = |0\rangle$ , and  $|\Psi(t_f)\rangle = -|2\rangle$  if  $w = 0$ . For the case where  $v = w$ , the state will be equally distributed between  $|0\rangle$  and  $|2\rangle$ .

The 3-site SSH chain in Fig. 4 is a bipartite tight-binding small chain with an imbalance in the number of sites on the sublattices, which implies the existence of a zero-energy eigenstate. Assuming that  $v$  is non-negative, the diagonalization of this system shows that the normalized zero-energy state is given by

$$|\Psi_0\rangle = \frac{w|0\rangle - v|2\rangle}{\sqrt{v^2 + w^2}}. \quad (8)$$

In this simple one-dimensional proposal, the authors designate the initially decoupled site as a defect or a domain wall that can be transferred along the SSH chain (if more dimers are present in the chain). As we will discuss in the next section, quantum gates can be constructed using the braiding of this defect in a three-chain configuration. Most importantly, if the transfer is slow, adiabaticity is preserved. This reflects that the defect state is, in fact, a zero-energy edge state in an SSH chain with a non-integer number of unit cells. In this case, an evolution where  $v$  is increased from 0 to 1 while  $w$  is having an opposite

decrease from 1 to 0 generates a transfer (with a  $\pi$ -phase shift) of the defect as shown in Fig. 4(c) while avoiding any energy level crossing (note that the energy gap between levels is  $\sqrt{v^2 + w^2}$ , which is finite as long as  $v$  and  $w$  are not simultaneously zero).

We now extend the same logic to the sine-cosine chain discussed in the previous section. The square-root construction that turns the parent Hamiltonian of a SSH chain into its square-root sine-cosine counterpart does not alter the underlying eigenstates, except for an overall phase or normalization factor. Let the parent Hamiltonian (SSH chain) be  $H_P$ , and its square-root counterpart (sine-cosine chain) be  $H_{\text{SR}}$ . The key relations are

$$H_{\text{SR}}^2 = \begin{pmatrix} H_A & 0 \\ 0 & H_B \end{pmatrix}, \quad (9)$$

where  $H_B$  is the SSH chain Hamiltonian with a global energy shift of 1,  $H_B = H_P + 1$ . An eigenstate  $|\psi_E\rangle$  of  $H_{\text{SR}}$  can be written as  $|\psi_E\rangle = \alpha|\phi_A\rangle + \beta|\phi_B\rangle$  where the amplitudes  $\alpha$  and  $\beta$  belong to the two decoupled sublattices. Because  $H_P$  has a protected zero-energy mode  $|\Psi_0\rangle$ , the corresponding defect state in the bipartite  $H_{\text{SR}}$  has energy  $\varepsilon = \pm 1$  and is given by

$$|\psi_{\varepsilon=\pm 1}\rangle = \frac{1}{\sqrt{2}}(|\Psi_A\rangle \pm |\Psi_0\rangle), \quad (10)$$

where  $|\Psi_A\rangle = H_{\text{SR}}|\Psi_0\rangle$ . Thus, the parent defect eigenstate maps onto one of the sublattice components of the defect eigenstates of the square-root chain, up to a phase. This reasoning can be extended to higher roots of the SSH chain with an increasing dilution of the SSH amplitudes as shown in Fig. 5.

During a quasi-adiabatic evolution, where the hopping angles  $\theta_j(t)$  change slowly, the adiabatic theorem guarantees that a system prepared in an eigenstate of the parent Hamiltonian will remain in that instantaneous eigenstate if energy levels do not cross (see details in Appendix B), accumulating only a dynamical and Berry phase. Because the eigenvector of the parent Hamiltonian (with energy  $(E^{(\text{SR})})^2 - 1$ ) coincides with a sublattice part of an eigenvector of the square-root Hamiltonian (with energy  $E^{(\text{SR})}$ ), the adiabatic trajectory of the parent Hamiltonian is inherited by the square-root system. Recall that the zero-energy defect state employed in the transfer protocol of the SSH parent maps into a larger defect state of energy  $\varepsilon = \pm 1$  of the Matryoshka chain as shown in Fig. 5. The protocol, therefore, works unchanged, modulo the additional phase that naturally arises during the evolution, that is, the  $H_{(1)}$  Matryoshka chain stays in the corresponding instantaneous defect eigenstate throughout the process. Note however that the additional zero-energy defect state due to the sublattice imbalance in the square-root chain evolves independently and is not related to the time evolution of the defect states of the parent Hamiltonian.

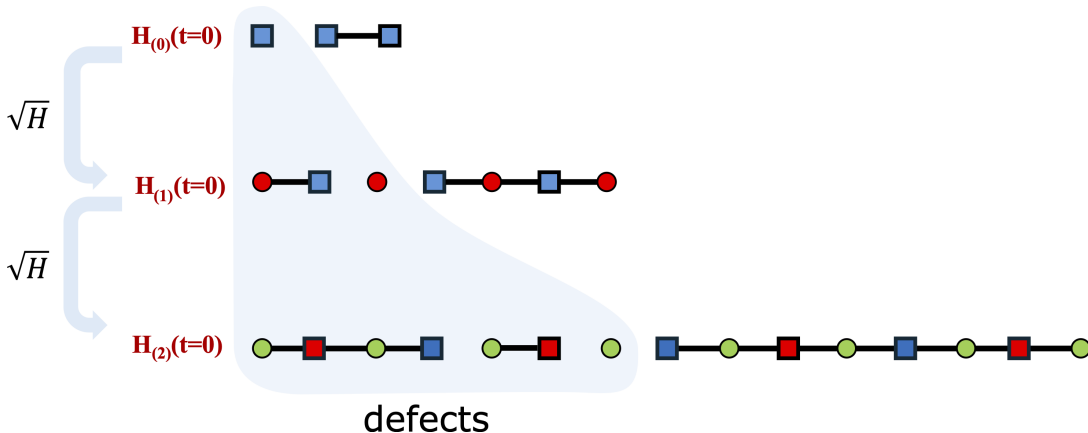


Figure 5: Consecutive square root of the initial Hamiltonian in the quantum transfer process. The highlighted defect state ( $H_{(1)}$ ) corresponds to the parent Hamiltonian's full chain ( $H_0$ ), where single-site, dimer, and 4-site cluster configurations are interchangeable under adiabatic evolution. The highlight shows the defect part in each model and, curiously, the defect in the square-root chain is the previous full chain (note that the ordering of the single site, the dimer and 4-site cluster can be exchanged under an adiabatic evolution).  $H_{(1)}(t=0)$  corresponds to  $\theta_{1,i} = \pi/2$ ,  $\theta_{2,i} = 0$ , and  $\theta_{3,i} = \lambda$ . In the first chain, we have one angle, in the second, we have three, and in the third, we have seven (see Appendix A for details). The amplitudes of the original 3-site SSH chain eigenstates will be present in the blue sites of all chains, except for eigenstates that result from the zero energy eigenstates of  $H_{(1)}$ ,  $H_{(2)}$ , etc.

Choosing an quasi-adiabatic evolution (large  $T$ ) of  $H_{(1)}$  with initial and final configurations as  $\theta_{1,i} = \theta_{2,f} = \pi/2$ ,  $\theta_{2,i} = 0$ ,  $\theta_{3,f} = \gamma$ ,  $\theta_{3,i} = \lambda$ ,  $\theta_{1,f} = \frac{\pi}{2} - \lambda$ , where  $\gamma$  is 0 or  $\pi$ , the evolution of the defect states is shown in Fig. 6 (see also Appendix B). In what concerns the defect states of energy

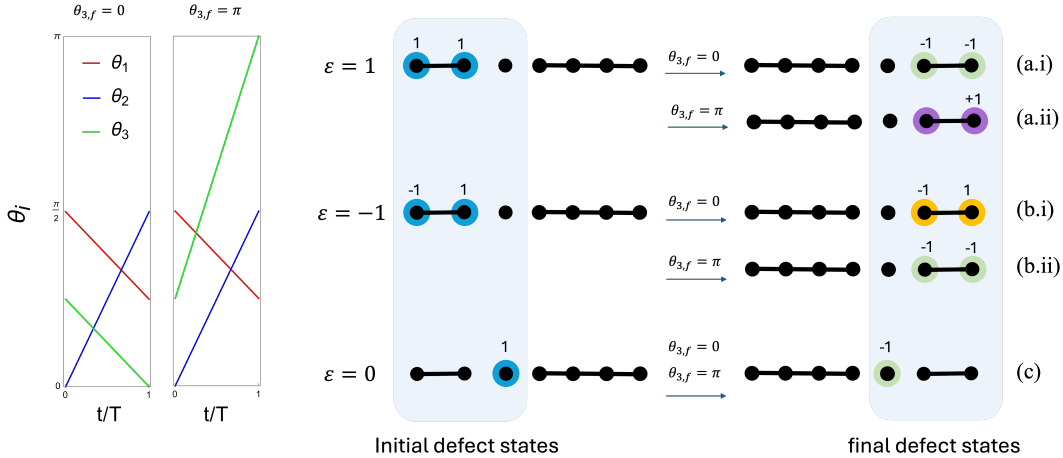


Figure 6: Simultaneous quasi-adiabatic quantum transfer of three energy states ( $\varepsilon = 1, -1$ , and  $0$ ) in a Matryoshka chain. Panels (a–c) correspond to  $\varepsilon = 1, -1$ , and  $0$ , respectively, with each panel showing two scenarios: (i)  $\theta_{3,f} = 0$  and (ii)  $\theta_{3,f} = \pi$ . The normalization constant was omitted for clarity. The left subplot illustrates the time evolution of angles  $\theta_1$ ,  $\theta_2$ , and  $\theta_3$  (red, blue, green lines), while the middle and right subplots depict the initial and final defect states.

$\varepsilon = \pm 1$ , signs in evolution in one sublattice are the same as in the previous parent chain, but relative signs in the other sublattice are fixed by the choice of  $0$  or  $\pi$ . The zero-energy defect state has support only in the outer sublattice and therefore is unrelated to the SSH defect state. This protocol transfers identically the defect states of the Matryoshka chain, with the only additional effect being a global phase factor that depends on the energy of the transferred state. This guarantees that the three defect states  $\varepsilon = \{+1, -1, 0\}$  can be simultaneously moved from one end of the chain to the other without loss of fidelity, provided the evolution is slow enough. Obviously, any combination of the 3 states (a qudit state with 3 components) will also be transferred. We will see in the next section that this allows us to define generalized qudit quantum gates.

Note that in Fig. 5, the highlighted defect of  $H_1$  corresponds to the parent Hamiltonian's full chain ( $H_0$ ), and so on. Also the single-site, dimer, and 4-site cluster parts of the defect are interchangeable under an adiabatic evolution.

## 4 Quantum Gates

Gate-operation scalability is fundamental as the number of qubits grows in a quantum computer implementation, with decoherence times that exceed the time required to perform operations on large qubit numbers [24, 25, 26]. This requirement poses a challenge, since the quantum gate must act slowly to ensure quantum transfer is performed under adiabatic conditions, as discussed in the previous section. In this section, we build on the previous discussion of quantum transfer in the Matryoshka chain and extend the braiding approach presented in [18] to construct scalable, topological quantum gates and test their performance under various types of disorder. Following the approach presented in [18], we use defects as carriers of qudit states and a Y-junction architecture [27].

In topological quantum computing, braiding refers to the adiabatic exchange of defects with non-commuting operations [20]. Because two defects cannot be interchanged along a single chain, a Y-junction architecture is adopted [27]. Braiding is achieved by adiabatically tuning the hopping amplitudes within each Y-junction leg, which drifts the defects without altering their energy. The Y-junction geometry allows one defect to remain stationary while the other traverses the junction, completing the exchange while the system stays in equilibrium throughout.

In Fig. 7, the braiding protocol proposed in [18] is illustrated on the top. The defect states undergoing the braiding process are represented in distinct colors: the left defect state  $|L\rangle$  is highlighted in yellow, while the right defect state  $|R\rangle$  appears in green. These topologically protected defect states form

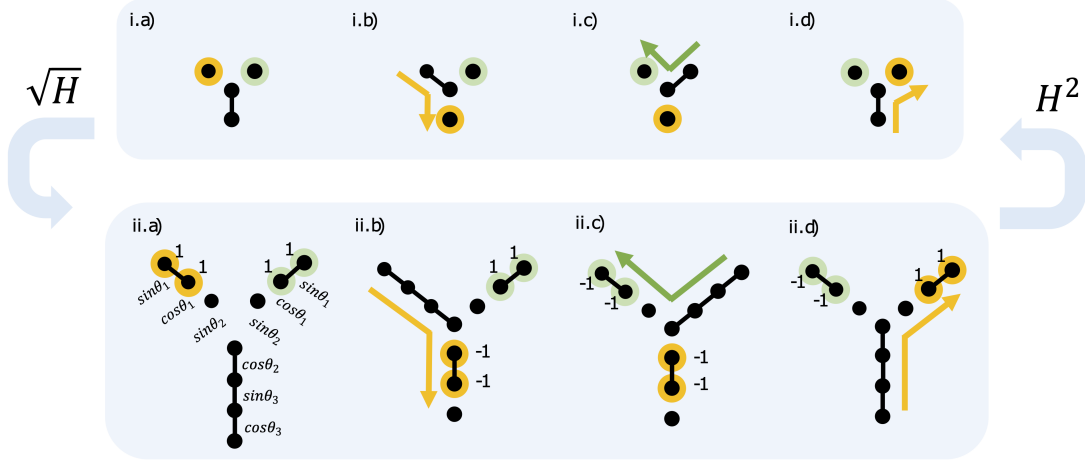


Figure 7: Braiding process in a (i) SSH-like and (ii) sine-cosine Y-junction. (i.a) Initial state with yellow (defect 1) and green (defect 2) circles. (i.b) and (i.c) show adiabatic transfer along semi-chains, with arrows indicating direction and phase factors accumulated during transfer. (i.d) Final configuration after defect exchange. (ii.a)–(ii.d) depict the corresponding square-root Matryoshka chain parameters and phase accumulations. The protocol follows [18] and the gate operation is described by Eq. 4.9 using the Matryoshka sine-cosine chain. We assumed  $\theta_{3,f} = 0$ .

the computational basis of the qubit system, with the qubit basis defined as  $\{|R\rangle, |L\rangle\}$ . During each transfer step, the defect states retain their initial energy due to the system’s chiral symmetry, while acquiring phase factors that depend on the transfer path. This phase accumulation is a critical feature of the braiding process, as it enables the implementation of non-trivial quantum operations. The braiding operation transforms the state  $|L\rangle$  into  $|R\rangle$ , while  $|R\rangle$  evolves into  $-|L\rangle$ . This transformation corresponds to a Y gate operation. This braiding protocol can be extended to implement the remaining  $X$  and  $Z$  Pauli gates by employing four SSH semi-chains.

Following the approach presented in the previous section, we replace the standard SSH Y-junction with a sine-cosine Matryoshka Y-junction, reflecting a square root of the former as explained in the previous section (see Fig. 7). Recall that now each defect supports three eigenstates with energies  $\varepsilon = \pm 1$  and  $\varepsilon = 0$ . In Fig. 7, we illustrate the braiding of the  $\varepsilon = 1$  defect states in the case  $\theta_{3,f} = 0$  (a  $\pi$  phase factor is present in each two-leg state transfer), which is determined by the hopping angles as described in Eq. 22. The phases acquired in this braiding are a direct consequence of the parent system accumulated phases in its braiding process.

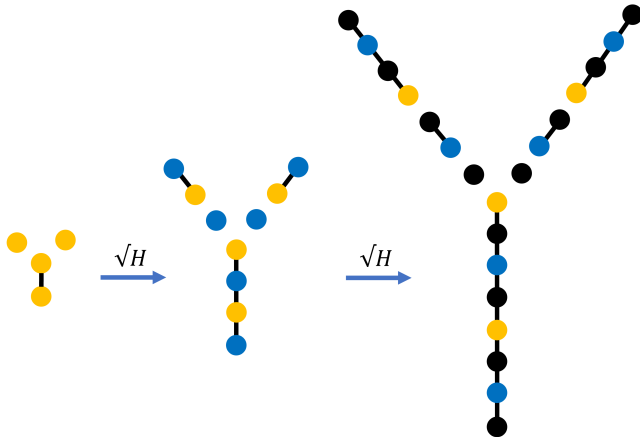


Figure 8: Scalable Y-junction quantum gate design using Matryoshka-type chains. Successive square-root operations ( $\sqrt{H}$ ) generate higher-order structures with generalized defects, each supporting  $2^N - 1$  distinct states for chain order  $N$  ( $N = 1, 2, 3, \dots$ ). The diagram illustrates the progressive nesting of defects across three hierarchical levels.

Considering the particular case of the Y-junction with 3-site defects, we consider the following subspace where the quantum information is coded, that is, where the qudit state is defined,

$$|1\rangle = |\varepsilon = 1; L\rangle = \frac{1}{\sqrt{2}} [1 \ 1 \ 0 \ \dots]^T \quad (11) \quad |4\rangle = |\varepsilon = -1; R\rangle = \frac{1}{\sqrt{2}} [\dots \ 0 \ 1 \ -1]^T \quad (14)$$

$$|2\rangle = |\varepsilon = 1; R\rangle = \frac{1}{\sqrt{2}} [\dots \ 0 \ 1 \ 1]^T \quad (12) \quad |5\rangle = |\varepsilon = 0; L\rangle = \frac{1}{\sqrt{2}} [0 \ 0 \ 1 \ \dots]^T \quad (15)$$

$$|3\rangle = |\varepsilon = -1; L\rangle = \frac{1}{\sqrt{2}} [1 \ -1 \ 0 \ \dots]^T \quad (13) \quad |6\rangle = |\varepsilon = 0; R\rangle = \frac{1}{\sqrt{2}} [\dots \ 1 \ 0 \ 0]^T \quad (16)$$

In the case of the Matryoshka braiding of Fig. 7, the full transfer operator can be expressed in this set of defect states as

$$\mathbf{OP} = \begin{bmatrix} e^{-it/\hbar} \begin{pmatrix} 0 & -1 \\ 1 & 0 \end{pmatrix} & \mathbf{0}_{2 \times 2} & \mathbf{0}_{2 \times 2} \\ \mathbf{0}_{2 \times 2} & e^{it/\hbar} \begin{pmatrix} 0 & 1 \\ 1 & 0 \end{pmatrix} & \mathbf{0}_{2 \times 2} \\ \mathbf{0}_{2 \times 2} & \mathbf{0}_{2 \times 2} & \begin{pmatrix} 0 & -1 \\ 1 & 1 \end{pmatrix} \end{bmatrix} = \begin{bmatrix} e^{-it/\hbar} Y_{\varepsilon=1} & \mathbf{0}_{2 \times 2} & \mathbf{0}_{2 \times 2} \\ \mathbf{0}_{2 \times 2} & e^{it/\hbar} X_{\varepsilon=-1} & \mathbf{0}_{2 \times 2} \\ \mathbf{0}_{2 \times 2} & \mathbf{0}_{2 \times 2} & Y_{\varepsilon=0} \end{bmatrix}, \quad (17)$$

which shows that an advantage of using the Matryoshka model instead of an SSH chain is its ability to compose gate operations.

A process is considered adiabatic when a given system evolves slowly compared with the timescale associated with the inverse of the energy level differences, and thus the energy levels' separations in the Hamiltonian's spectrum are preserved over time [28]. To preserve adiabatic conditions during the quantum state transfer, any change of the (i) on-site, (ii) off-site, or (iii)  $\theta_i$  parameters, must be occur smoothly. Fig. 9(a) shows a smooth time-dependent disorder, where a spline interpolates 20 disordered values around the original  $\theta$  curve, with a standard deviation of  $\sigma = 0.1$ . This scenario is realistic, assuming that in practice the perturbations acting on the system have weak time dependence.

We examine three types of disorder with smooth time-dependence to evaluate the performance of the gate protocol based on Matryoshka-type chains. The disorder types considered are: (i) on-site (diagonal) disorder, (ii) off-diagonal (hopping) disorder, and (iii) correlated off-diagonal disorder applied to the angles  $\theta_j$ . We start with the initial state  $|\Psi_0\rangle = (|\varepsilon = 1, L\rangle + |\varepsilon = 1, R\rangle)/\sqrt{2}$ , which evolves into  $|\Psi_f\rangle = (-|\varepsilon = 1, L\rangle + |\varepsilon = 1, R\rangle)/\sqrt{2}$  after the gate operation, following the sequence shown in Fig. 7. We numerically calculate the entropy and fidelity using perturbations smoothed with spline interpolation.

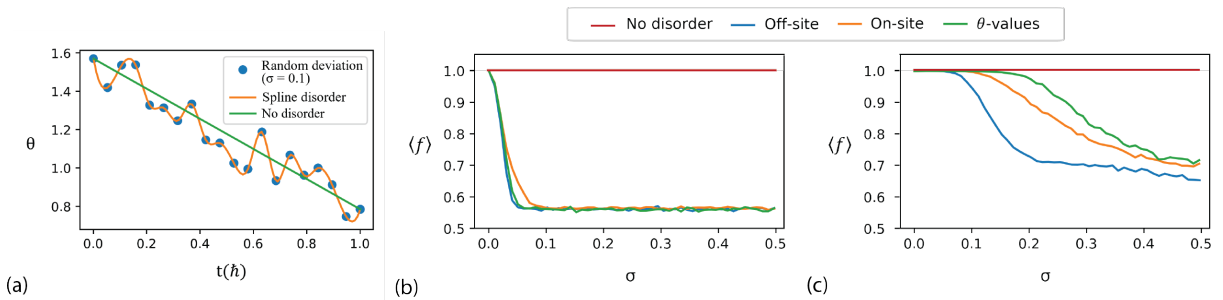


Figure 9: (a) Smooth disorder introduced using a spline interpolation over 20 random deviations sampled from a normal distribution with  $\sigma = 0.1$ . The green curve corresponds to the original, disorder-free evolution, while the orange and blue represent noisy evolutions. (b,c) Results for  $N = 1000$  transfers of the state  $|\Psi_0\rangle = (|\varepsilon = 1, L\rangle + |\varepsilon = 1, R\rangle)/\sqrt{2}$  to  $|\Psi_f\rangle = (-|\varepsilon = 1, L\rangle + |\varepsilon = 1, R\rangle)/\sqrt{2}$ , using the hopping configuration with  $\gamma = 0$  shown in Fig. 6 and smoothed (spline-interpolated) disorder in a total transfer time of  $3T(\hbar)$ . (b) Average fidelity; (c) Entropy values.

For both cases, we average the results over  $N = 1000$  disorder realizations at each point during a period  $3T$  [see Fig. 9(b)]. Since the gate protocol essentially consists of three consecutive state transfers, the results follow the same trend as for a single state transfer. However, fidelity and entropy change more rapidly due to the cumulative effect of errors at each stage. This reduces the duration of the plateau where the fidelity stays around  $F = 1$  before it drops and the state becomes mixed. Among the three types of disorder, case (ii) hopping disorder leads to the most rapid decay in fidelity. In contrast, case (iii) is the most stable and maintains the fidelity above  $F = 0.9$  for the longest time, since it evolves

correlated disorder in the angle parameters. The same trend is visible in entropy results, which translate into a rapid increase that reaches  $E = \ln 7$  very quickly, faster for case (ii) and slower for case (iii).

## 5 Quantum Memories

In this section, we construct a quantum memory based on the Matryoshka model by extending the protocol described in [19]. By adding more gaps through the Matryoshka construction, the number of protected eigenstates increases, allowing a larger set of qubits to be stored (or a high-dimensional qudit). Chiral symmetry plays a crucial role in preserving these topological properties throughout the whole chain [13].

We follow the transfer protocol introduced in [19] to move qubits into and out of the memory. A qubit is represented by two sites with an internal transition amplitude  $k$ . This qubit is initially disconnected from the memory chain and contains a single particle. The chain, which serves as the memory, couples to the qubit via a hopping term  $u$ . At the start of the protocol, the coupling is switched off; the particle resides in the qubit. When the coupling is turned on, the left site of the qubit and the first site of the chain form a two-state system that undergoes Rabi oscillations with period  $\tau_R = 2\pi/u$ . After a half-period  $t = \tau_R/2$ , the particle has migrated into the memory and remains there for a waiting time  $t_{\text{wait}}$ . To retrieve the qubit, the coupling is reopened, allowing another half-period of Rabi dynamics to transfer the particle back into the qubit. This sequence is illustrated in Fig. 10, which shows the initial placement of the particle, transfer into memory, the waiting interval, and final retrieval.

The fidelity of the transfer hinges on aligning the qubit's energy level with the edge-state energy of the chain; proper tuning of  $k$  and  $u$  maximizes overlap and suppresses leakage into bulk states. Under

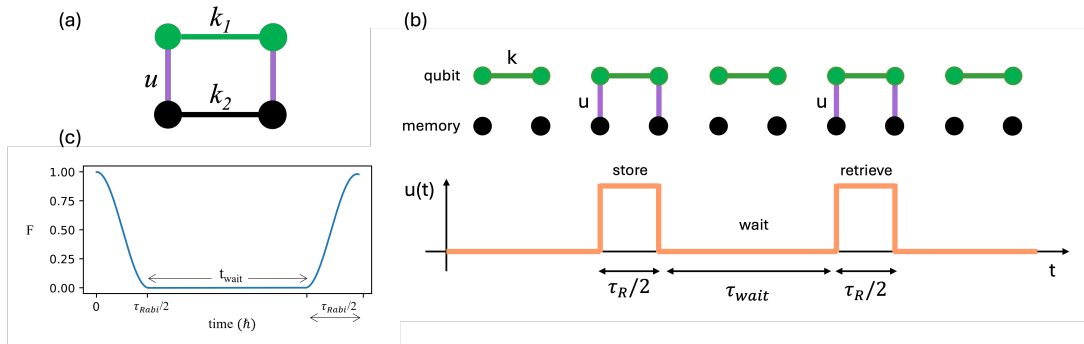


Figure 10: (a) Dot memory model showing two qubits with internal hopping terms  $k_1$  (green line) and  $k_2$  (black line). The qubits are connected through a coupling  $u$  (purple line). (b) Schematic representation from [19] of the qubit-memory transfer process. The particle is first stored in the memory after a Rabi half-period  $\tau_R/2$ , remains there during a waiting time  $t_{\text{wait}}$ , and is then retrieved back into the qubit over another interval of  $\tau_R$ . (c) Expected fidelity evolution during a perfect quantum state transfer of a qubit into a memory. The qubit hops into the memory after a period  $t_R/2$  and stays secured in the memory for a period  $t_{\text{wait}}$ . Then, it is transferred back after  $t_R/2$ .

perfect conditions, without any external disorder, we expect the fidelity to start at  $F = 1$  and decay to  $F = 0$  upon transfer to the memory. After a period  $t_{\text{wait}}$ , the fidelity goes back to  $F = 1$ , and we expect to have the same state as at the beginning of this protocol [see Fig. 10]. Starting from a trivial quantum memory model, the qubit state is transferred to the memory as described in Fig. 10. Each qubit has its own internal hopping term,  $k_1$  and  $k_2$  as shown. The qubit will be connected to the memory by a hopping term  $u$ , and the transfer time will depend on this parameter according to the Rabi time expression  $T = \tau_R/2 = \hbar/2u$ .

In [19], an SSH chain was proposed as a memory model, in which a qubit is connected to the end sites of the chain via hopping  $u$ . Simulations reveal that fidelity is maximized in the dimerized limit ( $v = 0$ ), where edge states are localized and protected, maintaining maximum fidelity ( $F = 1$ ). As the system moves away from this limit ( $v > 0$ ), edge states spread to neighboring sites, reducing transfer efficiency during  $\tau_R/2$  and causing weight transfer to dispersive states. This results in short-time, small-amplitude oscillations (due to dispersive state transfer) and long-time, large-amplitude oscillations (due to hybridization between the left and right states), with fidelity reaching zero. Additionally, stronger

transfer pulses (higher  $u$ ) improve efficiency, as evidenced by decreased fidelity decay for longer storage times, confirming that faster transfer to the memory enhances protocol efficiency.

Following the approach of the previous sections, we replace the SSH memory with a Matryoshka-type chain and keep one qubit with internal hopping  $k$  connected to the tips of the chain with absolute hopping  $u$ . We use a simple structure of type  $P = 1$  as illustrated in Fig. 11. The hopping parameters from the qubit to the chain are chosen according to the selected edge state where the qubit will be stored, see Figs. 11(b.i-iii).

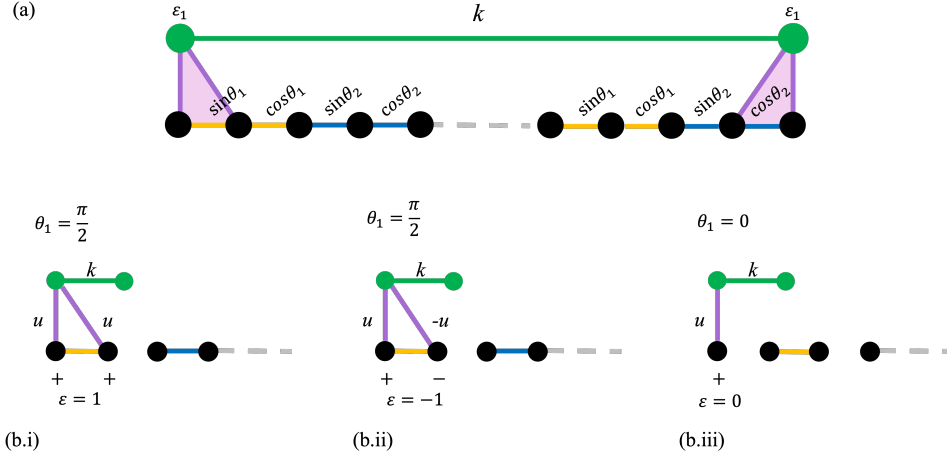


Figure 11: (a) Memory transfer model using one qubit connected to a Matryoshka chain of type  $P = 1$ . The qubit has internal hopping  $k$  (green line) and its connection to the memory depends on the energy of the edge state that will be used as memory. (b) Transferring method to different energy states. (b.i) Transfer of the qubit to the eigenstate with energy  $\epsilon = 1$  (symmetric combination). Requires  $\theta_1 = \pi/2$ . (b.ii) Transfer of the qubit to the eigenstate with energy  $\epsilon = -1$  (anti-symmetric combination). Requires  $\theta_1 = \pi/2$ . (b.iii) Transfer of the qubit to the eigenstate with energy  $\epsilon = 0$ . Requires  $\theta_1 = 0$ .

A chain with an odd number of sites, in the dimerized limit ( $\theta_1 = \pi/2$  and  $\theta_2 = 0$ ) will have a total of two edge states with energy  $\epsilon = -1$  (corresponding to anti-symmetric states localized at the first and last dimers of the chain), and two edge states with energy  $\epsilon = 1$  (corresponding to symmetric states localized at the first and last dimers of the chain) [see Fig. 12(a)].

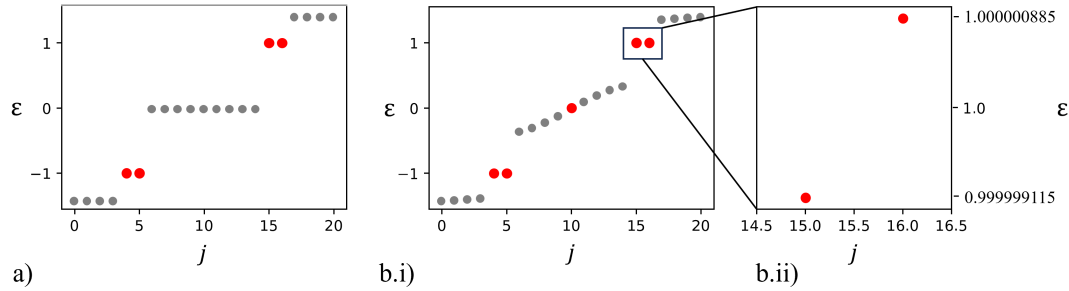


Figure 12: Energy spectrum of a Matryoshka chain with  $N = 21$  sites ( $P = 1$ ). (a) Edge-dimerized configuration with  $\theta_1 = \pi/2$  and  $\theta_2 = 0$ , showing degenerate edge states at energy  $\epsilon = \pm 1$ . (b.i) Non-edge-dimerized configuration with  $\theta_1 = 5\pi/12$  and  $\theta_2 = \pi/2 - \theta_1$ , where the degeneracy is lifted and state energies shift. (b.ii) Zoomed view of states near  $\epsilon = \pm 1$ , revealing a small energy splitting  $\Delta\epsilon \approx 1.77 \times 10^{-6}$  between formerly degenerate levels.

Two of the eigenstates with energy  $\epsilon = \pm 1$  will be localized at the leftmost part of the chain. To transfer an initial state  $|\Psi\rangle = |0\rangle$  of the qubit (corresponding to the particle localized at the left site), two connections should be present, so it transfers with equal weights to the symmetric or to the anti-symmetric states localized at the leftmost dimer [see Fig. 11(b.i) and b.ii)]. For the  $\theta_1 = 0$  case, there is one  $\epsilon = 0$  eigenstate fully localized at the first site of the chain, so the transfer only requires one connection [see Fig. 11(b.iii)].

The previously described cases consider chains with dimers at the edges, but if we choose different values for the hopping parameters, the edge states will no longer be fully localized to the leftmost and rightmost parts of the chain and will have decaying weights in the bulk. When slightly stepping away from this edge-dimer limit and considering values as  $\theta_1 = 5\pi/12$  and  $\theta_2 = \pi/2 - \theta_1$ , the degenerate edge states gain a small difference in energy [see Fig. 12(b)], reflecting a hybridization between the left and right edge states. In this scenario, we expect Rabi oscillations with a period of  $\tau_R = \pi/\Delta\varepsilon$ , so the previous fidelity values that would remain as  $F = 1$  for any  $t_{wait}$  will now vary for different values as we vary this parameter. This evolution matches the previously studied behaviour in an SSH chain, when stepping away from the dimerized limit [19]. Because of this edge state spreading, there is a weight transfer into the dispersive states when performing the transfer described by Fig. 11(a.i) and a.ii). Therefore the final fidelity value will vary with the storage time  $t_{wait}$ , exhibiting short-time oscillations of small amplitude and long-time oscillations of large amplitude as shown in 13(a). To achieve higher fidelity, we could keep the state in memory for a sufficient amount of time so that an integer number of oscillations occur, allowing most of the amplitude to return to the initial two sites. In Fig. 13,  $t_{wait}$ , we study the impact of the storage time variation  $t_{wait}$  on the values of fidelity. Due to the hybridization of the edge states, the energy difference between the symmetric and anti-symmetric states visible in Fig. 12(b.ii) can be used to predict the expected fidelity decay to zero  $\tau_R/2 = \pi/2\Delta\varepsilon$ . In the inset in Fig. 13(a) we observe the

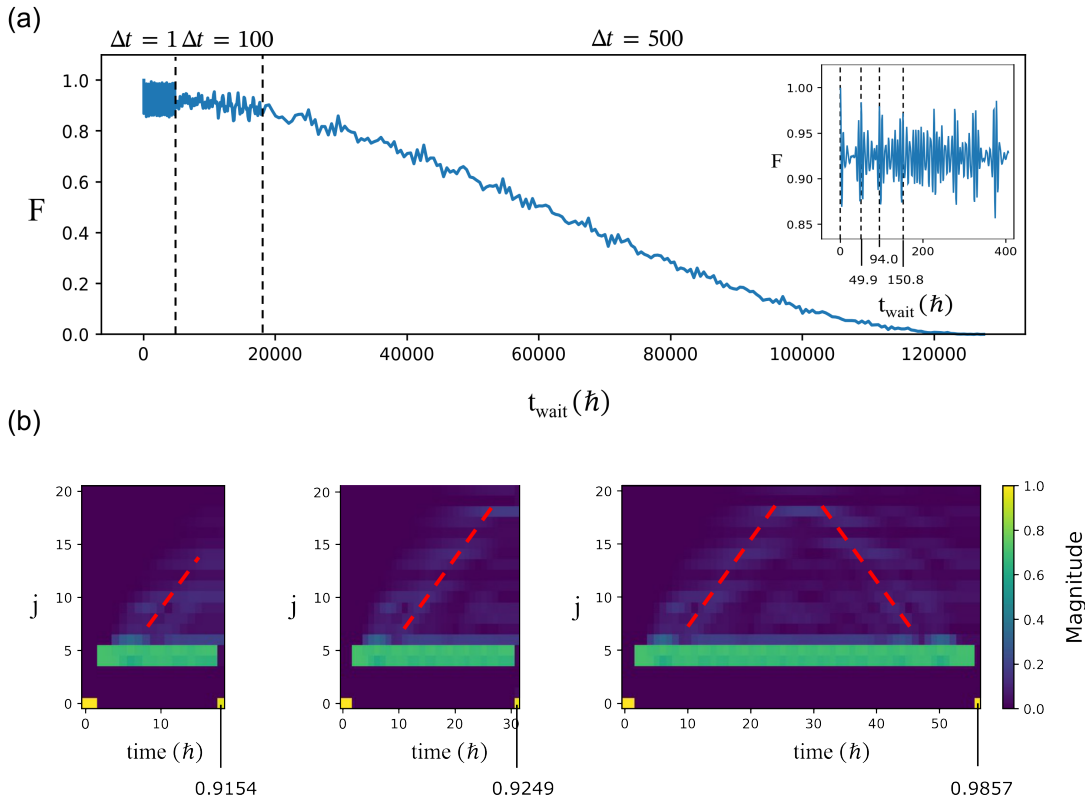


Figure 13: (a) Fidelity  $F$  versus storage time  $t_{wait}$  in a Matryoshka chain with 21 sites ( $P = 1$ ,  $\theta_1 = \pi/12$ ,  $\theta_2 = \pi/2 - \theta_1$ ). The plot displays half of the large-amplitude fidelity oscillation, corresponding to quantum state transfer from the left edge state to the right edge state. Three regions with different sampling times are separated by vertical dashed lines. Inset: Zoomed view near  $t_{wait} = 0$ , highlighting the first four peaks (including  $t_{wait} = 0$ ) where maximum fidelity is reached, indicated by vertical dashed lines. (b) Density plots of the quantum state for storage times before and close to the second fidelity peak. The initial state  $|\Psi_0\rangle = |k = 0\rangle$  is symmetrically transferred to the leftmost two sites, stored for duration  $t_{wait}$ , then transferred back to the qubit with expected result  $|\Psi_f\rangle = |k = 0\rangle$ . Final fidelity values are shown in the bottom-right corners of each image.

fidelity reaches periodic maximum values with its first peak at instant  $t_{wait} = 49.9$ . This period matches the time evolution of the state density localization in Fig. 13(b). The triangle path illustrated by the dashed red line in those figures reflect this fidelity oscillation and we can see that after a time interval around 50, the state is nearly back to the initial configuration. This will match the first peak in the

fidelity evolution in Fig. 13(a).

## 6 Conclusion

Scalability remains one of the most critical challenges in realizing practical quantum computers, particularly in terms of physical resource overhead and error mitigation. This work proposes a simple approach toward scalable topological quantum computing. This approach relies on a particular hierarchical lattice structure, the Matryoshka-type Sine-Cosine chain, that allows the encoding of high-dimensional qudits within a single topological system. Unlike conventional architectures that require physical isolation for each qubit, the  $2^n$ -root construction of these models allows multiple edge states and energy gaps to coexist, reducing the resource footprint of multi-qubit encoding operations.

We showed that in these systems, it is possible to implement scalable quantum gates using Y-junction braiding. This braiding relies on the adiabatic transfer of generalized defects across semi-chains following the approach of [18]. These gates exhibit partial topological protection against local perturbations, reflecting the robustness of the scalable transfer protocols to various forms of disorder (on-site, off-diagonal, and correlated angle disorder). While errors accumulate across multiple quantum state transfer operations, fidelity remains above  $F = 0.9$  for significant disorder ranges under adiabatic conditions.

We also described the integration of Matryoshka chains into quantum memory architectures, which allow for the storage of quantum information in multiple protected edge states simultaneously. Our analysis shows that memory fidelity remains high over extended periods and the quantum memory capacity scales with the order  $P$  of the chain, enabling multi-qubit or qudit storage within a single device.

Experimental realization of these systems is possible using photonic waveguides fabricated via femtosecond laser writing, which allows precise control over hopping parameters and effective simulation of the discrete quantum system [29, 30, 31, 32, 33]. Additionally, classical implementations such as topolectrical circuits [34, 35, 36] and acoustical lattices [37, 38, 39] present promising platforms for testing the behavior of these scalable architectures.

## Acknowledgements

This work was developed within the scope of Portuguese Institute for Nanostructures, Nanomodelling and Nanofabrication (i3N) Projects No. UIDB/50025/2020, No. UIDP/50025/2020, and No. LA/P/0037/2020, financed by national funds through the Fundação para a Ciência e Tecnologia (FCT) and the Ministério da Educação e Ciência (MEC) of Portugal. A.M.M. acknowledges financial support from i3N through the work Contract No. CDL-CTTRI-91-SGRH/2024. G.F.M. acknowledges financial support from FCT through the grant BI/UI96/12758/2025.

## Appendix A: Quantum transfer in sine-cosine chains

This appendix shows how quantum state transfer protocols based on three-site SSH chains also apply to Matryoshka-type chains, as their square-root Hamiltonians preserve SSH eigenstates as sublattice amplitudes. We detail the adiabatic evolutions of the hopping parameters to move defects and acquire controlled phase shifts, demonstrating this is a scalable method for transferring a large number of quantum states within the topological framework.

The sine-cosine chains are bipartite, therefore the Hamiltonian can be written using the chiral basis  $\{|A\rangle, |B\rangle\}$  as

$$H = \begin{bmatrix} 0 & H_{AB} \\ H_{BA} & 0 \end{bmatrix}, \quad (18)$$

where

$$|A\rangle = \sum_{i=1}^{N_A} \alpha_i |A_i\rangle, \quad \text{where } |A_i\rangle = |2(i-1)\rangle, \quad (19)$$

and  $N_A$  is the number of sites of type  $A$ , while  $|B\rangle = \sum_{i=1}^{N_B} \beta_i |B_i\rangle$  is a vector with non-zero values only at the  $B$  sublattice, with  $|B_i\rangle = |2i-1\rangle$ . The respective eigenvalue equation can also be written as  $H_{AB}|A\rangle = \varepsilon|B\rangle$  and  $H_{BA}|B\rangle = \varepsilon|A\rangle$ .

Considering now the square root of the three-site base structure represented in Fig. 4 as  $H_{(1)}$ , the defect present there consists of the group of the three leftmost sites. Throughout the defect transfer,  $H_{(1)}$  will always host  $\varepsilon = 1$  and  $\varepsilon = -1$  states which result from the square root of the  $H_{(0)}$  zero-energy state. Using the relation between parent and square-root Hamiltonians (see Fig. 14), and the form of the  $H_{(0)}$  zero-energy state

$$|B\rangle = [\cos \theta, 0, -\sin \theta]^T = [\cos \theta_2 \sin \theta_3, 0, -\cos \theta_1 \sin \theta_2]^T, \quad (20)$$

the state  $|A\rangle$  can be inferred from  $|B\rangle$ ,

$$|A\rangle = [\beta_1 \sin \theta_1, \beta_1 \cos \theta_1 + \beta_2 \sin \theta_2, \beta_2 \cos \theta_2 + \beta_3 \sin \theta_3, \beta_3 \cos \theta_3]^T. \quad (21)$$

When site  $A_1$  and  $B_1$  are connected by a hopping term  $\sin \theta_1 = 1$  and site  $A_2$  is isolated, the  $H_{(1)}$  defect eigenstates will be  $|\Psi_{\varepsilon=0}\rangle = |A_2\rangle$ ,  $|\Psi_{\pm}\rangle = (|A_1\rangle \pm |B_1\rangle)/\sqrt{2}$ . In this case, the initial form of state  $|B\rangle$  is  $|B_i\rangle = [1, 0, 0]$ , while the final form is  $|B_f\rangle = [0, 0, -1]$ . So by setting the connections as

$$\theta_{1,i} = \theta_{2,f} = \pi/2, \quad \theta_{2,i} = 0, \quad \theta_{3,f} = \gamma, \quad \theta_{3,i} = \lambda, \quad \theta_{1,f} = \frac{\pi}{2} - \lambda, \quad (22)$$

the global state can be written as

$$\begin{aligned} |\Psi_{\pm,i}\rangle &= \frac{1}{\sqrt{2}} [\pm 1, 1, 0, 0, 0, 0]^T, \\ |\Psi_{\pm,f}\rangle &= \frac{1}{\sqrt{2}} [0, 0, 0, 0, 0, -1, \mp \cos \gamma]^T, \end{aligned} \quad (23)$$

which means that if  $\gamma = 0$ , a phase shift of  $\pi$  will occur for  $\varepsilon = 1$ , but not for  $\varepsilon = -1$  (see Fig. 6). However when  $\gamma = \pi$ ,  $\varepsilon = 1$  will generate an antibonding state from an initial bonding state, and a  $\pi$  phase shift will occur when  $\varepsilon = -1$  (see Fig. 6). The same results for  $|B\rangle$  hold when sites  $B_1$  and  $A_2$  are connected in the defect and  $A_1$  is isolated, but since the following connections change to  $\theta_{1,i} = \theta_{2,i} = 0$ ,  $\theta_{2,f} = \pi/2$ , the global state becomes

$$|\Psi_{\pm,i}\rangle = \frac{1}{\sqrt{2}} [0, \pm 1, 1, 0, 0, 0]^T. \quad (24)$$

In general, when the eigenstates have a finite value of energy ( $\varepsilon = \pm 1$ ), the final state will acquire a dynamic phase factor  $e^{\pm i T/\hbar}$ , but for the zero-energy state, this phase is cancelled.

Additionally, since this structure is a bipartite lattice with a sublattice imbalance, there also will be a zero energy state with support at sublattice  $A$ , while all  $B$  sites will have zero weight. Assuming that  $A_1 = 1$  and applying the eigenvalue equation of the tight-binding model, then

$$|A\rangle = [1, -\tan \theta_1, \tan \theta_1 \tan \theta_2, -\tan \theta_1 \tan \theta_2 \tan \theta_3]^T. \quad (25)$$

This means that if the connection evolution is set as (see Fig. 6)

$$\theta_{1,i} = \theta_{2,f} = \pi/2, \quad \theta_{2,i} = \theta_{3,f} = 0, \quad \theta_{3,i} = \gamma, \quad \theta_{1,f} = \pi/2 - \gamma \quad (26)$$

the state will evolve from  $|\Psi_i\rangle = |2\rangle$  to  $|\Psi_f\rangle = -|5\rangle$ , acquiring a  $\pi$ -phase. The same will occur if  $\theta_{3,f} = \pi$  (see Fig. 6).

These reasoning can be consecutively applied to the chain  $H(n)$  obtained from its squared version  $H(n-1)$  (see Fig. 14). Therefore, one can develop a protocol for transferring a large number of defect states, while taking advantage of the protection inherited by the sine-cosine chain.

## Appendix B: Robustness to disorder and level crossing

In this appendix, we discuss the robustness of quantum transfer protocols against disorder and level crossing. We show that, without a minimum gap between Hamiltonian eigenvalues, weight transfer occurs during evolution, compromising the fidelity of the state-transfer process.

To ensure the adiabatic condition is preserved, the energy levels of the system Hamiltonian should be separated by a minimum gap, since when the levels get closer, there is a transfer of weight between the respective Hamiltonian eigenstates. Without any disorder, considering the quantum transfer evolution of Fig. 6 with  $\gamma = 0$ , the initial state  $|\Psi_0\rangle = (|1\rangle + |2\rangle)/\sqrt{2}$  will simply evolve to the expected state

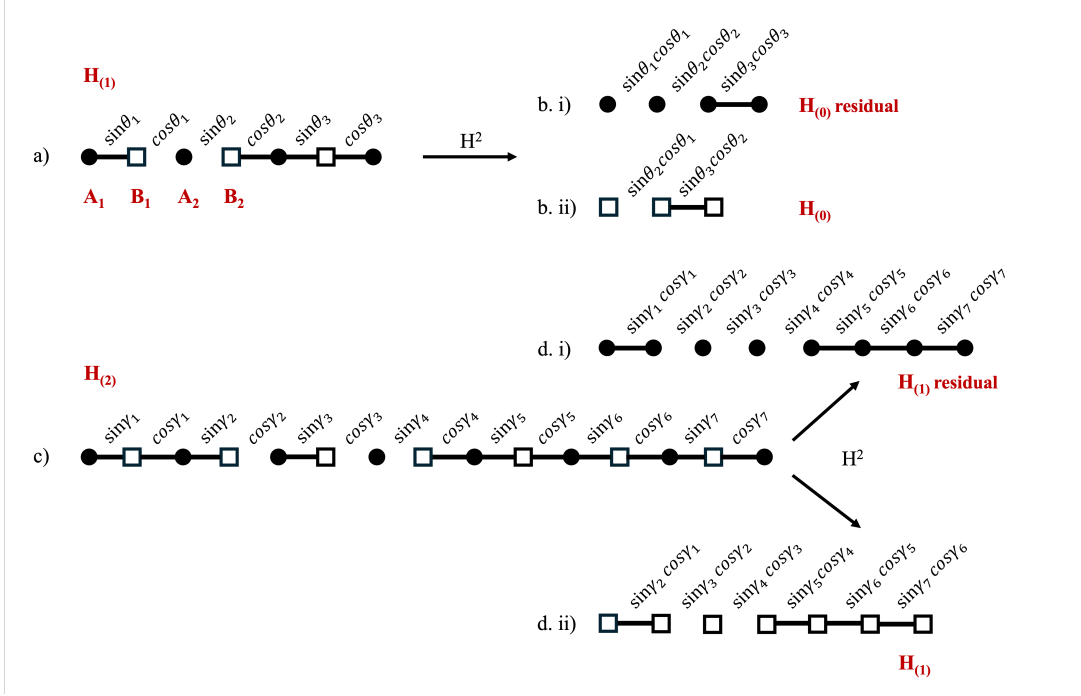


Figure 14: Recursive squaring of Matryoshka lattices. Squaring the Hamiltonian  $H_{(1)}$  (a) yields a residual structure (b.i) and the parent structure (b.ii). Similarly, squaring  $H_{(2)}$  (c) produces a parent structure (d.ii) identical to (a), and the residual structure (d.i). On-site terms are omitted.

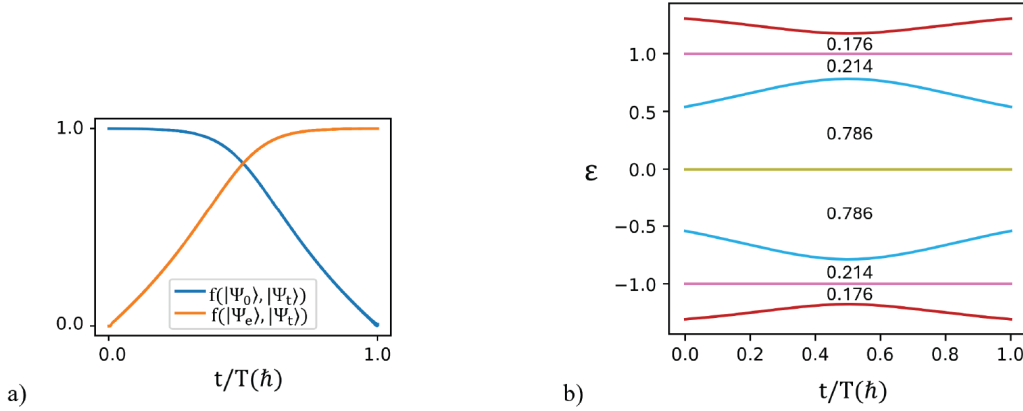


Figure 15: Evolution of  $\Psi_0$  under  $H_{(1)}$  without disorder using Eq. 22 hopping values. (a) Blue line shows fidelity evolution compared to initial state  $|\Psi_0\rangle$ , orange line shows fidelity compared to expected state  $|\Psi_e\rangle$ . (b) Energy spectrum during complete state transfer, where  $T$  represents total transfer time.

$|\Psi_e\rangle = -(|6\rangle + |7\rangle)/\sqrt{2}$ , with the fidelity between the initial state and the expected state smoothly transitioning from  $F = 1$  to  $F = 0$ , keeping the energy levels well separated during this evolution, as expected for a Matryoshka-type structure. Without any external interferences, the average fidelity value is maintained close to 1, and the energy levels are separated by minimum energy values of 0.786, 0.214, and 0.176 (see Fig. 15). By introducing Gaussian disorder, for example, in the  $\theta$  parameter values, the energy levels begin to move closer to each other until they cross [see Fig. 16(a)]. This effect is stronger when disorder is applied on-site, and the levels cross sooner [see Fig. 16(b)]. We can also observe in Fig. 16 that fidelity starts to decrease for disorder applied on the  $\theta$  parameters when  $\sigma > 0.3$ , due to level crossing.

To illustrate these negative effects caused by level crossing on state transfer, we will below focus only on two states  $|\epsilon_i(t)\rangle$  and  $|\epsilon_j(t)\rangle$  [with  $\epsilon_i(t)$  intersecting  $\epsilon_j(t)$  at some instant], while ignoring the weight transfer to the other states (assumed to be well separated in energy from the pair). Considering

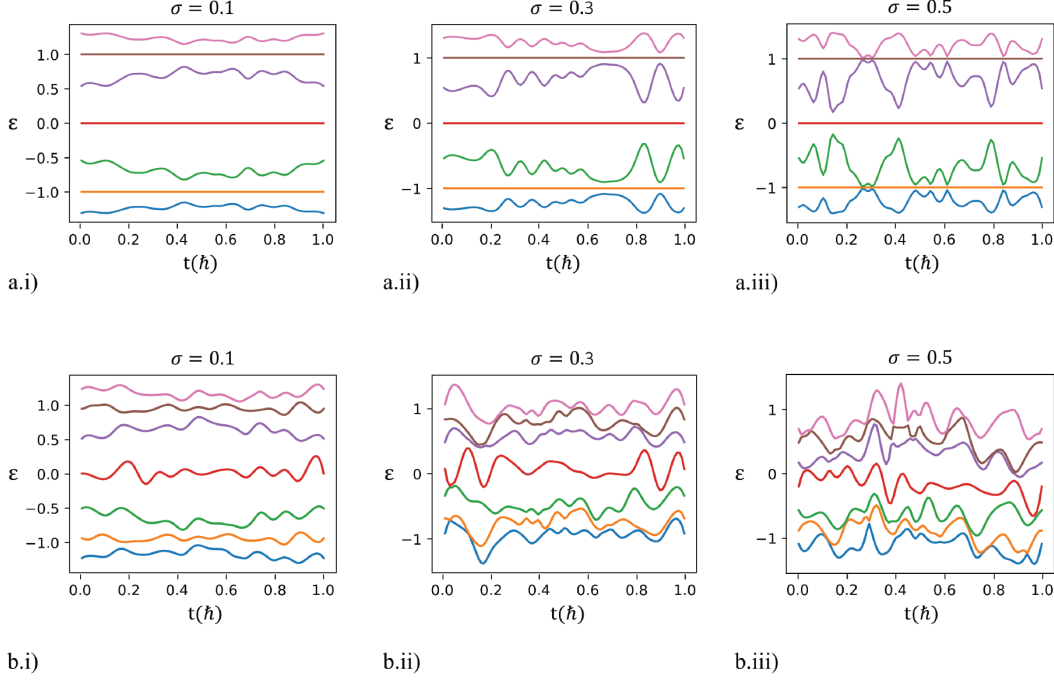


Figure 16: Evolution of the energy spectrum under increasing levels of Gaussian disorder applied on the  $\theta$  parameters: a.i), a.ii), and a.iii):  $G(0, \sigma = 0.1, \theta)$ ,  $G(0, \sigma = 0.3, \theta)$ , and  $G(0, \sigma = 0.5, \theta)$ . As disorder grows, the levels move closer together and eventually cross, leading to stronger mixing between states. b.i), b.ii), and b.iii): Disorder applied to on-site energies.

for now the general case of a time-dependent Hamiltonian with an arbitrary number of levels and a time-dependent eigenstate basis  $\{|\epsilon_i(t)\rangle\}$ , the time evolution of a state can be written as

$$|\Psi(t)\rangle = \sum_j \alpha_j(t) |\epsilon_j(t)\rangle. \quad (27)$$

So using the time-dependent Schrödinger equation (with  $\hbar = 1$ ), one has

$$iH(t) |\Psi(t)\rangle = \frac{d}{dt} |\Psi(t)\rangle = \sum_j \frac{d\alpha_j(t)}{dt} |\epsilon_j(t)\rangle + \sum_j \alpha_j(t) \frac{d}{dt} |\epsilon_j(t)\rangle. \quad (28)$$

The projection of this equation into  $|\epsilon_i(t)\rangle$  leads to

$$\frac{d\alpha_i}{dt} = -i\epsilon_i(t)\alpha_i(t) - \sum_j \alpha_j \langle \epsilon_i(t) | \frac{d}{dt} |\epsilon_j(t)\rangle. \quad (29)$$

This equation can be written as a sum of the diagonalized Hamiltonian  $H_d$  plus the projection matrix  $D_{ij} = \frac{d\langle \epsilon_i |}{dt} |\epsilon_j\rangle$  associated with the rotation of the eigenstates,

$$\frac{d\Psi}{dt} = (-iH_d + D)\Psi, \quad (30)$$

where

$$\Psi = \begin{bmatrix} \alpha_1(t) \\ \alpha_2(t) \\ \vdots \end{bmatrix}; \quad H_d = \begin{bmatrix} \epsilon_1(t) & & \\ & \epsilon_2(t) & \\ & & \ddots \end{bmatrix}; \quad D = \begin{bmatrix} -\langle \epsilon_1 | \frac{d}{dt} |\epsilon_1\rangle & -\langle \epsilon_1 | \frac{d}{dt} |\epsilon_2\rangle & \dots \\ -\langle \epsilon_2 | \frac{d}{dt} |\epsilon_1\rangle & & \\ \vdots & & \ddots \end{bmatrix}. \quad (31)$$

Considering adiabatic conditions  $\Delta\epsilon_{ij} \gg D_{ij}$ ,  $D$  acts as a perturbation to the system, and the state evolution is determined mainly by  $H_d$ , resulting in an approximately constant value of  $|\alpha_i|$ . However,

when the two levels cross, there are two degenerate states,  $\Delta\varepsilon_{ij} = 0$ , and the projection term then dominates the evolution, causing an exchange of weight between states  $i$  and  $j$ .

The coupling between the two states can be reduced to a toy model [40], and the state evolution can be understood as a coherent oscillation in an effective two-level system. This evolution can be represented on a Bloch sphere, where it is driven by a rotation Hamiltonian

$$\mathbf{H} = \frac{1}{2}\mathbf{n} \cdot \boldsymbol{\sigma}, \quad (32)$$

with  $\mathbf{n} = (n_x, n_y, n_z)$  as the unit vector, which dictates the rotation axis of the state vector. To show this, we use the density matrix of a qubit

$$\rho(t) = \frac{1}{2}(\mathbb{I} + \mathbf{r}(t) \cdot \boldsymbol{\sigma}), \quad (33)$$

where  $\mathbf{r}(t)$  is the Bloch vector representing the qubit's state at time  $t$ . From the relation  $\langle \sigma_i \rangle = \text{Tr}(\rho(t)\sigma_i) = r_i(t)$ , we find

$$\mathbf{r}(t) = \langle \Psi(t) | \boldsymbol{\sigma} | \Psi(t) \rangle. \quad (34)$$

Differentiating with respect to time yields

$$\begin{aligned} \frac{d}{dt}\mathbf{r}(t) &= \frac{d}{dt}\langle \Psi(t) | \boldsymbol{\sigma} | \Psi(t) \rangle = \langle \Psi'(t) | \boldsymbol{\sigma} | \Psi(t) \rangle + \langle \Psi(t) | \boldsymbol{\sigma} | \Psi'(t) \rangle = \\ &= i\langle \Psi'(t) | \mathbf{H}(t) \boldsymbol{\sigma} | \Psi(t) \rangle - i\langle \Psi(t) | \boldsymbol{\sigma} \mathbf{H}(t) | \Psi'(t) \rangle = i\langle \Psi(t) | [\mathbf{H}(t), \boldsymbol{\sigma}] | \Psi(t) \rangle. \end{aligned} \quad (35)$$

The commutator is evaluated using the Hamiltonian from equation 32 and the Pauli matrix commutation relation  $[\sigma_i, \sigma_j] = 2i\varepsilon_{ijk}\sigma_k$ ,

$$[\mathbf{H}(t), \boldsymbol{\sigma}] = \frac{1}{2}[\mathbf{n}(t) \cdot \boldsymbol{\sigma}, \boldsymbol{\sigma}] = i(\mathbf{n}(t) \times \boldsymbol{\sigma}), \quad (36)$$

where  $\varepsilon_{ijk}$  is the Levi-Civita symbol. Using equation 34, we conclude that the evolution of  $\mathbf{r}(t)$  follows a precessional motion around the vector  $\mathbf{n}(t)$ ,

$$\frac{d}{dt}\mathbf{r}(t) = -\langle \Psi(t) | \mathbf{n}(t) \times \boldsymbol{\sigma} | \Psi(t) \rangle = \mathbf{n}(t) \times \mathbf{r}(t). \quad (37)$$

When the energy levels of the system cross at a given instant, a degeneracy occurs. The eigenvalues of the Hamiltonian are given by  $\varepsilon_{\pm} = \pm\frac{1}{2}|\mathbf{n}(t)|$ , and the energy gap between the two bands is  $\Delta\varepsilon = |\mathbf{n}(t)|$ . Thus,  $\Delta\varepsilon \rightarrow 0$  as  $\mathbf{n}(t) \rightarrow 0$ . The vector  $\mathbf{n}(t)$  governs the rotation of the state vector, such that when  $\mathbf{n}(t) \rightarrow 0$ , the state vector no longer follows the direction of  $\mathbf{n}(t)$ . This causes the state vector to acquire a larger angular distance in the Bloch sphere in relation to the  $\mathbf{n}(t)$  direction. As  $\mathbf{n}(t)$  returns to a nontrivial vector, the system experiences an abrupt drop in fidelity, as the state vector rapidly re-aligns itself with the new direction defined by  $\mathbf{n}(t)$ . This weight transfer results from the vanishing of the energy gap, which leads to a mixing of the eigenstates and a breakdown of the simple precessional motion of the state vector around a fixed axis.

To exemplify this effect, we use the case with a Gaussian disorder with a value of  $\sigma = 0.35$ , applied to the on-site energies of the Matryoshka chain Hamiltonian. Figs. 17(a.ii) and (b.ii) illustrate the sharp fidelity decrease at the moment when two of the spectrum levels cross in Fig. 17(c.ii). The precession motion is also evident in the oscillations of the fidelity values, which demonstrate the exchange of weights between the two higher-energy eigenstates.

## Appendix C: N-qubit or qudit memory

In the main text, a single qubit transfer was performed to a quantum memory using the Matryoshka chain. This appendix explains how to extend that protocol to qudit memory, where higher-dimensional quantum information can be stored within the same topological framework. The key advantage is that a high-dimensional qudit (or equivalently, multiple qubits) can be encoded into the edge states of a single physical chain, reducing hardware overhead while maintaining partial topological protection.

The method described in Section 5 may be used to sequentially transfer a qudit with, for example, 4 components, or equivalently, a 2-qubit state, to the edge states. One possible approach involves shifting the energies of each qubit sites as shown in Fig. 18 and weakly couple the qubits and the chain so that

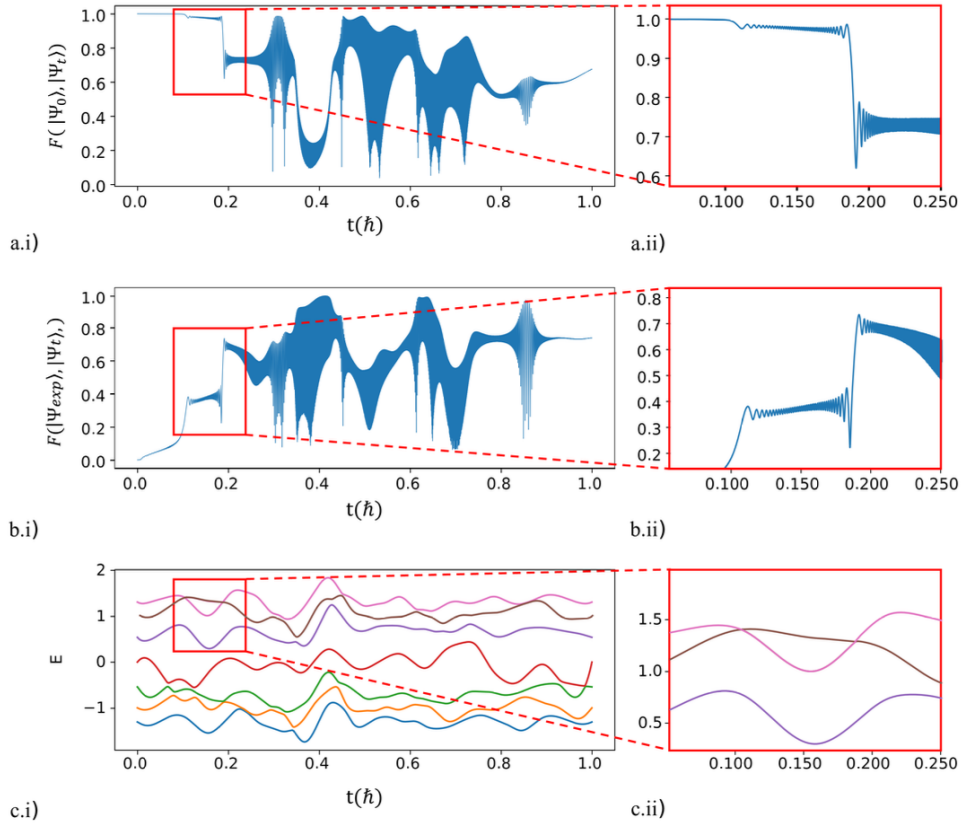


Figure 17: (a,b) Fidelity evolution of a quantum state with energy initially at  $\varepsilon = 1$  of a disordered Matryoshka chain system, with connections defined by Eq. 22. (c) The energy spectrum of the chain. Plots show (a.i) the fidelity relative to the initial state, (b.i) fidelity relative to the expected final state, and (c.i) the time evolution of energy spectrum. The corresponding insets (a.ii, b.ii, and c.ii) highlight critical regions: fidelity loss during precession near degeneracy points and level crossings that correspond to the observed drops in fidelity.

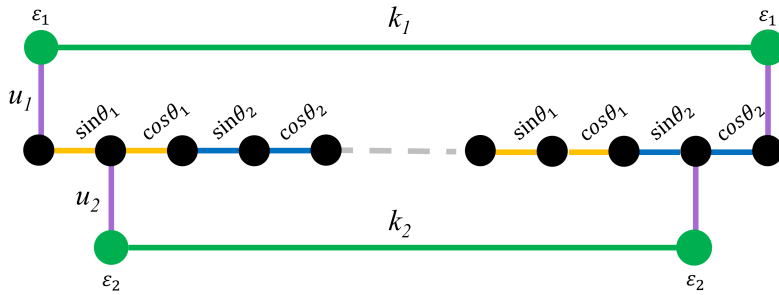


Figure 18: Memory transfer model using a 4-component qudit corresponding to 2 qubits connected to a Matryoshka chain of type  $P = 2$ , with sine-cosine coupling strengths between memory sites (black and white circles). Each pair of qudit sites has internal hopping amplitudes  $k_1$  and  $k_2$  (green lines) and is connected to the memory with hoppings  $u_1$  and  $u_2$  (purple lines).

the qubit state is transferred to the edge states with same energy. However, this method requires long transfer times and precise energy tuning. A more efficient alternative is to extend the protocol from Section IV by rapidly transferring a higher-dimensional qudit directly to a Matryoshka  $P = 2$  chain choosing particular connection configurations that select the edge states where we want to store the qubit state, as shown in Fig. 11. This transfer process is applied separately for each qubit.

This can be done also with Sine-Cosine chains that deviate from the exact Matryoshka form, for

example, one may consider a Sine-Cosine  $P = 2$  chain with connection values determined by  $\theta_1 = \pi/6$ ,  $\theta_2 = \pi/4$ ,  $\theta_3 = \pi/6$ ,  $\theta_4 = 0$ . This configuration produces the spectrum shown in Fig. 19 in the case of a chain with 80 sites. We have a left defect with 7 sites and a right one with 7 sites. In total, there are 14 edge states in the system, so our qudit Hilbert space has dimension  $d = 14$ . These defect energy levels are represented in Fig. 19 in colors yellow, blue, and green, following the same color scheme as in Fig. 3(c).

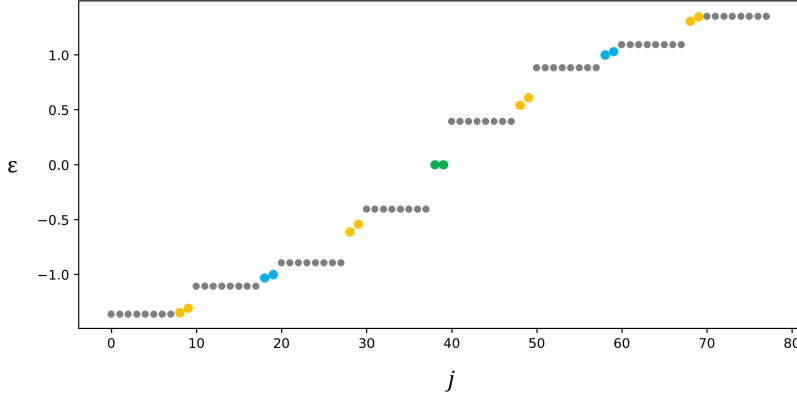


Figure 19: Energy spectrum  $\varepsilon$  as a function of the site index  $j$  for a Matryoshka-like chain of type  $P = 2$  with connection angles  $\theta_1 = \pi/6$ ,  $\theta_2 = \pi/4$ ,  $\theta_3 = \pi/6$ , and  $\theta_4 = 0$ . The system contains 80 sites, resulting in left and right defects of 7 sites each. The colored points (yellow, blue, and green) correspond to the localized defect states, following the same color scheme as in Fig. 3(c).

From the diagonalization of the left defect Hamiltonian, we can obtain for example the defect eigenstate with energy  $\varepsilon = 0$ :

$$|\psi_{\varepsilon=0}\rangle = [1, 0, -\tan(\pi/6), 0, -\tan(\pi/6)\tan(\pi/4), 0, -\tan^2(\pi/6)\tan(\pi/4)]^T. \quad (38)$$

These weight values (scaled by a constant  $u$ ) serve as hopping parameters to transfer a qubit into this state of the memory, as illustrated in Fig. 20. On the right side of the chain, the respective defect state

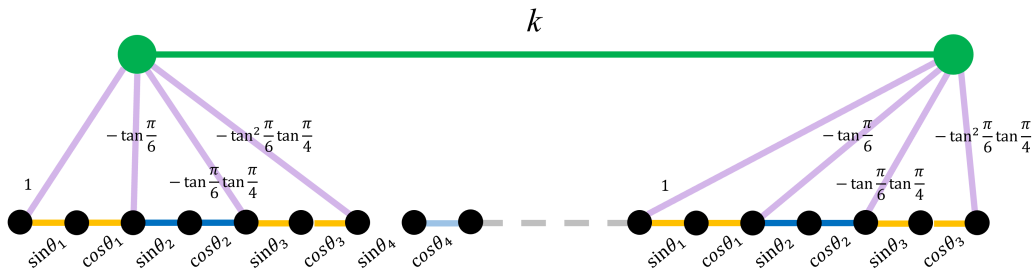


Figure 20: Controlled localization and transfer of a qubit to defect states of the quantum memory using a Matryoshka-type lattice with connection angles  $\theta_1 = \pi/6$ ,  $\theta_2 = \pi/4$ ,  $\theta_3 = \pi/6$ , and  $\theta_4 = 0$  and 80 sites. The transfer protocol ensures adiabatic evolution while maintaining topological protection of the stored quantum information.

will have approximately the same form.

This qudit (or multiple qubit) memory architecture exponentially scales with the order  $P$  of the Matryoshka chain.

## References

- [1] W. H. Zurek, “Decoherence and the transition from quantum to classical,” *Physics Today*, vol. 44, no. 10, pp. 36–44, 2003.

- [2] P. W. Shor, “Scheme for reducing decoherence in quantum computer memory,” *Physical review A*, vol. 52, no. 4, p. R2493, 1995.
- [3] J. Clarke and F. K. Wilhelm, “Superconducting quantum bits,” *Nature*, vol. 453, no. 7198, pp. 1031–1042, 2008.
- [4] E. Gibney, “Quantum computer quest,” *Nature*, vol. 516, no. 7529, pp. 24–27, 2014.
- [5] A. G. Fowler, M. Mariantoni, J. M. Martinis, and A. N. Cleland, “Surface codes: Towards practical large-scale quantum computation,” *Physical Review A—Atomic, Molecular, and Optical Physics*, vol. 86, no. 3, p. 032324, 2012.
- [6] P. W. Shor, “Fault-tolerant quantum computation,” in *Proceedings of 37th conference on foundations of computer science*. IEEE, 1996, pp. 56–65.
- [7] A. Y. Kitaev, “Fault-tolerant quantum computation by anyons,” *Annals of physics*, vol. 303, no. 1, pp. 2–30, 2003.
- [8] C. Nayak, S. H. Simon, A. Stern, M. Freedman, and S. Das Sarma, “Non-Abelian anyons and topological quantum computation,” *Reviews of Modern Physics*, vol. 80, no. 3, pp. 1083–1159, 2008.
- [9] M. Ezawa, “Systematic construction of square-root topological insulators and superconductors,” *Phys. Rev. Res.*, vol. 2, p. 033397, 2020-09. [Online]. Available: <https://link.aps.org/doi/10.1103/PhysRevResearch.2.033397>
- [10] J. Arkininstall, M. Teimourpour, L. Feng, R. El-Ganainy, and H. Schomerus, “Topological tight-binding models from nontrivial square roots,” *Physical Review B*, vol. 95, no. 16, p. 165109, 2017.
- [11] A. Marques and R. Dias, “ $2n$ -root weak, chern, and higher-order topological insulators, and  $2n$ -root topological semimetals,” *Phys. Rev. B*, vol. 104, no. 16, p. 165410, 2021.
- [12] A. M. Marques, L. Madail, and R. G. Dias, “One-dimensional  $2^n$ -root topological insulators and superconductors,” *Phys. Rev. B*, vol. 103, p. 235425, 2021-06. [Online]. Available: <https://link.aps.org/doi/10.1103/PhysRevB.103.235425>
- [13] R. G. Dias and A. M. Marques, “Matryoshka approach to sine-cosine topological models,” *Phys. Rev. B*, vol. 103, p. 245112, 2021-06. [Online]. Available: <https://link.aps.org/doi/10.1103/PhysRevB.103.245112>
- [14] W. P. Su, J. R. Schrieffer, and A. J. Heeger, “Solitons in polyacetylene,” *Phys. Rev. Lett.*, vol. 42, pp. 1698–1701, Jun 1979. [Online]. Available: <https://link.aps.org/doi/10.1103/PhysRevLett.42.1698>
- [15] J. Zurita, C. E. Creffield, and G. Platero, “Fast quantum transfer mediated by topological domain walls,” *Quantum*, vol. 7, p. 1043, 2023.
- [16] F. M. d’Angelis, F. A. Pinheiro, D. Guéry-Odelin, S. Longhi, and F. Impens, “Fast and robust quantum state transfer in a topological su-schrieffer-heeger chain with next-to-nearest-neighbor interactions,” *Physical Review Research*, vol. 2, no. 3, p. 033475, 2020.
- [17] X.-Y. Zhang, Y. Yan, L.-N. Zheng, Z.-X. Zhang, L.-N. Zhong, S. Zhang, and H.-F. Wang, “Topological phase and tunable quantum state transfer of su-schrieffer-heeger chain with an embedded quantum ring,” *Advanced Quantum Technologies*, vol. 7, no. 8, p. 2400156, 2024.
- [18] P. Boross, J. K. Asbóth, G. Széchenyi, L. Oroszlány, and A. Pályi, “Poor man’s topological quantum gate based on the su-schrieffer-heeger model,” *Physical Review B*, vol. 100, no. 4, p. 045414, 2019.
- [19] A. Pályi, “Topological insulators 2: Ssh model and quantum memory (lecture 1),” Lecture notes, Budapest University of Technology and Economics, 2018, accessed: 2025-03-25. [Online]. Available: <http://eik.bme.hu/~palyi/TopologicalInsulators2-2018Spring/TopSup-Lecture01-SSHQuantumMemory.pdf>
- [20] E. Dennis, A. Kitaev, A. Landahl, and J. Preskill, “Topological quantum memory,” *Journal of Mathematical Physics*, vol. 43, no. 9, pp. 4452–4505, 2002.

- [21] C. Dłaska, B. Vermersch, and P. Zoller, “Robust quantum state transfer via topologically protected edge channels in dipolar arrays,” *Quantum Science and Technology*, vol. 2, no. 1, p. 015001, 2017.
- [22] F. Mei, G. Chen, L. Tian, S.-L. Zhu, and S. Jia, “Robust quantum state transfer via topological edge states in superconducting qubit chains,” *Physical Review A*, vol. 98, no. 1, p. 012331, 2018.
- [23] M. Estarellas, I. D’Amico, and T. Spiller, “Topologically protected localised states in spin chains,” *Scientific Reports*, vol. 7, p. 42904, 2017. [Online]. Available: <https://doi.org/10.1038/srep42904>
- [24] D. P. DiVincenzo, “The physical implementation of quantum computation,” *Fortschritte der Physik: Progress of Physics*, vol. 48, no. 9-11, pp. 771–783, 2000.
- [25] P. Estarellas, “Spin chain systems for quantum computing and quantum information applications,” Ph.D. dissertation, University of York, 2018.
- [26] M. A. Nielsen and I. L. Chuang, *Quantum computation and quantum information*. Cambridge university press, 2010.
- [27] M. Ezawa, “Non-abelian braiding of majorana-like edge states and topological quantum computations in electric circuits,” *Phys. Rev. B*, vol. 102, no. 7, p. 075424, 2020.
- [28] M. Born and V. Fock, “Beweis des adiabatenatzes,” *Zeitschrift für Physik*, vol. 51, no. 3, pp. 165–180, 1928.
- [29] S. Longhi, “Quantum-optical analogies using photonic structures,” *Laser & Photonics Reviews*, vol. 3, no. 3, pp. 243–261, 2009.
- [30] G. O. Pérez, J. M. Dueñas, D. Guzmán-Silva, L. E. F. Torres, and C. Hermann-Avigliano, “Transport of non-classical light mediated by topological domain walls in a ssh photonic lattice,” *Scientific reports*, vol. 14, no. 1, p. 12435, 2024.
- [31] D. Viedma Palomo, “Harnessing topology in photonic waveguide systems,” 2024.
- [32] P. Zhou, G.-G. Liu, Y. Yang, Y.-H. Hu, S. Ma, H. Xue, Q. Wang, L. Deng, and B. Zhang, “Observation of photonic antichiral edge states,” *Phys. Rev. Lett.*, vol. 125, p. 263603, Dec 2020. [Online]. Available: <https://link.aps.org/doi/10.1103/PhysRevLett.125.263603>
- [33] S. Li, Z.-Y. Xue, M. Gong, and Y. Hu, “Non-abelian aharonov-bohm caging in photonic lattices,” *Phys. Rev. A*, vol. 102, p. 023524, Aug 2020. [Online]. Available: <https://link.aps.org/doi/10.1103/PhysRevA.102.023524>
- [34] L. Song, H. Yang, Y. Cao, and P. Yan, “Realization of the square-root higher-order topological insulator in electric circuits,” *Nano Lett.*, vol. 20, no. 10, pp. 7566–7571, Oct. 2020. [Online]. Available: <https://doi.org/10.1021/acs.nanolett.0c03049>
- [35] S. Liu, W. Gao, Q. Zhang, S. Ma, L. Zhang, C. Liu, Y. J. Xiang, T. J. Cui, and S. Zhang, “Topologically protected edge state in two-dimensional su-schrieffer-heeger circuit,” *Research*, vol. 2019, p. 8609875, Feb. 2019. [Online]. Available: <https://doi.org/10.34133/2019/8609875>
- [36] C. H. Lee, S. Imhof, C. Berger, F. Bayer, J. Brehm, L. W. Molenkamp, T. Kiessling, and R. Thomale, “Topoelectrical circuits,” *Communications Physics*, vol. 1, no. 1, p. 39, Jul. 2018. [Online]. Available: <https://doi.org/10.1038/s42005-018-0035-2>
- [37] M. Yan, X. Huang, L. Luo, J. Lu, W. Deng, and Z. Liu, “Acoustic square-root topological states,” *Phys. Rev. B*, vol. 102, p. 180102(R), Nov 2020. [Online]. Available: <https://link.aps.org/doi/10.1103/PhysRevB.102.180102>
- [38] H. Xue, Y. Yang, F. Gao, Y. Chong, and B. Zhang, “Acoustic higher-order topological insulator on a kagome lattice,” *Nature Materials*, vol. 18, no. 2, pp. 108–112, Feb. 2019. [Online]. Available: <https://doi.org/10.1038/s41563-018-0251-x>
- [39] L.-Y. Zheng, V. Achilleos, O. Richoux, G. Theocharis, and V. Pagneux, “Observation of edge waves in a two-dimensional su-schrieffer-heeger acoustic network,” *Phys. Rev. Applied*, vol. 12, p. 034014, Sep 2019. [Online]. Available: <https://link.aps.org/doi/10.1103/PhysRevApplied.12.034014>
- [40] J. Gouveia, I. Maceira, and R. Dias, “Evolution of localized states in lieb lattices under time-dependent magnetic fields,” *Physical Review B*, vol. 94, no. 19, p. 195132, 2016.